Tin-lead Alloying for Efficient and Stable All-inorganic Perovskite Solar Cells

Journal:	*Chemistry of Materials*
Manuscript ID	cm-2019-04265e.R2
Manuscript Type:	Article
Date Submitted by the Author:	14-Mar-2020
Complete List of Authors:	Yang, Zuobao; Ningbo University of Technology, Institute of Materials Zhang, Xiaohong; Ningbo University of Technology Yang, Weiyou; Ningbo University of Technology, Institute of Materials Eperon, Giles; National Renewable Energy Laboratory, Ginger, David; University of Washington, Chemistry; University of Washington, Department of Chemistry

Tin-lead Alloying for Efficient and Stable All-inorganic Perovskite Solar Cells

Zuobao Yang,[†, #] Xiaohong Zhang, [‡, #] Weiyou Yang, [†] Giles E. Eperon, [§, ǁ, *] David S. Ginger [*, ǁ]

[†]Institute of Materials, Ningbo University of Technology, Ningbo, 315211, China
[‡]College of Science, Ningbo university of Technology, Ningbo, 315211, China
[§]Cavendish Laboratory, JJ Thomson Avenue, Cambridge CB3 0HE, UK
[ǁ]Department of Chemistry, University of Washington, Seattle, Washington 98195-1700, United States

ABSTRACT: Cesium containing all-inorganic perovskites have received considerable interest in photovoltaics research because of their potential for improved stability compared to their organic-inorganic hybrid counterparts. However, the inorganic perovskites studied thus far still suffer from lower power conversion efficiency and long-term instability, due to an unfavorable bandgap and either phase instability or air-sensitivity. Herein, A strategy to mitigate these concerns is investigated by alloying tin and lead on the B site to form tin-lead alloyed low-bandgap (~1.34 eV) inorganic $CsSn_{0.3}Pb_{0.7}I_3$ perovskites. Solar cells made using this material in an inverted full-structured architecture with a PEDOT:PSS hole transport materials (HTM) attain power conversion efficiency (PCE) up to 9.41% (stabilized PCE 7.23%). Furthermore, a simple HTM-free device without PEDOT:PSS layer is demonstrated more stable than the full-structured device and exhibits a PCE of 7.60% (stabilized PCE 7.31%) – the highest efficiency to date for an inorganic perovskite with a bandgap below 1.40 eV. This simplified device structure shows good reproducibility and stability. This work provides a possible route for fabricating low-cost, high stability devices with competitive efficiencies.

INTRODUCTION

In recent years, organic-inorganic hybrid halide perovskites have been the subject of much research due to their unique physical and chemical properties (e.g. large optical absorption, high mobility, long diffusion length),[1-3] as well as cost effectiveness and solution processability. As a result, dramatic improvements have been made to the power conversion efficiency (PCE) of the perovskite solar cells from 3.8% to 25.2%.[4-910] Although such high performance is beginning to rival commercial Si-based solar cells, the long-term stability of perovskites is still an active area of research as companies look towards commercialization on large scales.[11, 12] The best performing perovskite solar cells usually contain organic cations, such as methylammonium (MA^+) and formamidinium (FA^+),[13-18] which are both volatile under elevated temperature and susceptible to moisture-related degradation. One proposed route to address these problems is by replacing the organic cations with inorganic cations, such as cesium (Cs^+) or rubidium (Rb^+), to form all-inorganic perovskites;[19-21] these approaches have already demonstrated enhanced thermal stability, moisture resistance and photostability yet generally with lower overall performance than the hybrid counterparts.[22-25]

The first report of functioning all-inorganic perovskites in solar cells was by Snaith et al,[26] who demonstrated a power conversion efficiency (PCE) of 2.9% with cubic $CsPbI_3$ perovskites. Unfortunately, $CsPbI_3$ in the black cubic perovskite phase is unstable in ambient atmosphere and prone to transform into a yellow, orthorhombic non-perovskite phase,[19, 27-31] which is non-photoactive and deteriorates performance of the devices. Several strategies have been proposed to address this issues including solvent engineering,[23, 32] surface/volume ratio modulation,[33, 34] anion substitution, and others.[22, 27, 29, 35-41] Impressive enhancements have been achieved not only on the stability but also on the performance of the devices; very recently, all-inorganic perovskite PCEs of over 13% with improved stability have been reported by several groups.[23, 35, 36, 39] Such progress is encouraging, but the PCE of the inorganic perovskite solar cells are still inferior to that of the organic-inorganic counterparts. One reason for this limitation is that the bandgaps of the stable Cs-based perovskites lie in a range of 1.7-2.3eV, significantly above that for ideal single-junction solar cells (1.1-1.4eV). [22, 24, 28, 29, 35-38, 40-45]

A strategy that has been used very recently to tailor the bandgap for organic-containing perovskites is replacing Pb in the lattice with Sn, which results in a lower bandgap. Sn-based perovskites have been demonstrated with lower bandgap, high charge mobility, and being more eco-friendly than Pb-based perovskites.[46-48] However, fully Sn-based perovskites suffer from their notorious air-sensitivity because the Sn^{2+} tends to be oxidized to Sn^{4+}.[49, 50] A recent strategy that provides a route around this issue in organic-containing perovskites is alloying Sn and Pb. In organic-inorganic perovskites, tin-lead alloyed perovskites have been shown to have low bandgap but have oxidation stability more similar to Pb than Sn materials.[19, 51-58] Encouraged by these scenarios, we hypothesized that

incorporation of Sn^{2+} into an all inorganic lead halide perovskite would broaden the spectral response of inorganic cesium lead iodide and exhibit enhancement of the PCE and stability.

In this work, we prepare all-inorganic tin-lead perovskites by a facile solution process. Alloying Sn and Pb provides a strategy to mitigate the limitations of all-inorganic perovskites; first, tin-lead alloying gives rise to bandgap bowing, allowing us to reach bandgaps that are ideal for PV operation (~1.34 eV). Second, the incorporation of Sn stabilizes the perovskite structure by increasing the tolerance factor of the lattice, which results in superior phase stability. With this composition we attain power conversion efficiencies of 9.41% in an inverted full-structured device architecture, competitive for all-inorganic perovskites, and in a more stable HTM-free architecture we are still able to achieve 7.60% PCE and stabilized 7.31% PCE. These results are both the most efficient HTM-free all-inorganic perovskite, and, most importantly, the most efficient low-bandgap (E_g < 1.40 eV) inorganic perovskite solar cell to the best of our knowledge. Notably, the un-capsulated inorganic tin-lead perovskite solar cells exhibit good photostability under continuous illumination, long-term stability and the air stability. Tin-lead alloyed all-inorganic perovskite thus represent a promising avenue to stable and efficient devices, which could be used in both single junction and tandem solar cells.

EXPERIMENTAL SECTION

Materials:

All materials were used as received without purification as follows: PbI_2 (Alfa Aesar, 99.999%), SnI_2 (Alfa Aesar, 99.999%), CsI (Sigma-Aldrich, 99.999%), SnF_2 (Acros Organics, 99%), PEDOT:PSS (Ossila, Al4083), $PC_{61}BM$ (Solenne, 99.5%), Bathocuproine(BCP)(alfa Aesar, 98%), N,N-Dimethylformamide (DMF)(Sigma-Aldrich, anhydrous, 99.8%), dimethyl sulfoxide (DMSO)(Sigma-Aldrich, anhydrous, >99.9%), chlorobenzene(Sigma-Aldrich, anhydrous, 99.8%), 2-propanol (IPA)(Sigma-Aldrich, anhydrous, 99.5%), anisole (Sigma-Aldrich, anhydrous, 99.7% and ITO.

Materials synthesis:

Tin-lead precursors. The tin-lead mixed compounds were prepared by dissolving stoichiometric amount of SnI_2, PbI_2, CsI for the desired composition in an aqueous mixed solvent (DMF:DMSO =7:3 v/v)s with a small amount of SnF_2 (SnI_2:SnF_2=1:0.1 in molar ratio) at a constant stirring at ~60 °C overnight. In a typical $CsSn_{0.3}Pb_{0.7}I_3$, for example, 322.7 mg PbI_2, 117.8 mg SnI_2, 4.7 mg SnF_2 and 259.8 mg CsI were mixed in 1 mL mixed solvent (700 uL DMF and 300 uL DMSO) to obtain 1 M precursor. For $MASn_{0.3}Pb_{0.7}I_3$, the CsI was replaced with MAI counterparts All the products were filtered with 450 μm PTFE filter before use.

CsPbI2Br precursor. PbI_2, $PbBr_2$ and CsI were dissolved in a mixed solvent (DMF:DMSO=7:3 v/v) in the appropriate molar ratios to result a 0.43 M precursor solution of $CsPbI_2Br$, which was stirred overnight at 150 °C and filtered before use.

Device fabrication.

The pre-patterned ITO substrates were ultrasonically cleaned in diluted Micro-90 detergent, deionized water, acetone and 2-propanol bath sequentially, and dried with nitrogen. Prior to thin film deposition, the substrates were treated for 20 min with oxygen plasma or UV/O_3. For inverted full-structured devices, a thin layer of PEDOT:PSS was deposited and then heated at 150 °C for 15 min on a hotplate before transferring into a nitrogen-filled glovebox. For HTM-free devices, the cleaned ITO substrates were transferred into the glovebox for films deposition immediately after oxygen plasma or UV/O_3 treatment. The compositional inorganic perovskite precursors were spin-coated onto the substrates at 10000 rpm for 1s with acceleration rate of 11000rpm and 0 rpm for 20 s with acceleration rate of 500 rpm sequentially in the glovebox. The resulted substrates were annealed at 100 °C for 20 min (it depends on the retention time of black films for that with molar ratio of Sn/Pb less than 0.30) on a hotplate. The perovskite-coated substrates were immersed into an anti-solvent anisole solution for 20 s. Afterwards, PCBM (20 mg mL^{-1} in anhydrous chlorobenzene) and BCP (0.5 mg mL^{-1} in anhydrous IPA) were sequentially spun on the substrates at 2000 rpm for 20 s and 6000 rpm 15s, respectively. Finally, silver electrode (~100 nm) was deposited by thermal evaporation to complete the fabrication.

Device characterization.

The photocurrent density-voltage curves and stabilized power output of the devices were measured in the glovebox using a Keithley 2400 source meter under AM 1.5G solar illumination at 100 mW cm^{-2}. External quantum efficiency (EQE) measurements were performed in ambient environment by loading the samples in a vacuum chamber using a xenon arc lamp and a monochromator, which the light intensity was calibrated with a standard Si photodiode. For devices stability testing, all the samples were transferred out from the glovebox and exposed in air without encapsulation.

X-ray diffraction (XRD). XRD characterization was carried out on perovskite thin films on the glass substrates using a Bruker D8 Advance powder diffraction meter with Cu Kα radiation under operation conditions of 40 kV and 44 mA.

X-ray/ultraviolet photoelectron spectroscopy (XPS/UPS). The sample for XPS/UPS was obtained by spin-coating the precursor solution on ITO substrate. The XPS measurements were carried out in an ultrahigh vacuum of ~$6*10^{-11}$ mbar using a Kratos AXIS Ultra DLD. The sample was transferred into the vacuum chamber as soon as possible and excited with X-rays from a monochromatic Al Kα source. High-resolution XPS spectra were fitted with CasaXPS package. UPS characterization was performed in the same chamber as for XPS using a He 1 α source at 21.22 eV. The electron binding energy scale was calibrated using the Fermi edge of clean gold.

UV-Vis absorption. Optical absorption spectra were recorded for perovskite thin films deposited on glass substrates in ambient environment using Agilent 8453 Diode Array UV-Vis spectrophotometer. Sample temperature is controlled from within ChemStation software via an external temperature controller which drives a Peltier heat pump attached to the sample holder. For the films with molar ratio of Sn/Pb less than 0.30, the UV-vis absorption spectra were also obtained using an AvaSPec-ULS2048XL-EVO spectrometer in the glovebox.

Photoluminescence and time resolved photoluminescence (PL/TRPL). The steady-state photoluminescence of the samples was performed by placing the sample in a vacuum chamber. Samples were photoexcited using a 450 nm light-emitting diode (LED) and the signals were recorded using a home-built setup based on an Ocean-Optics 2000+ spectrometer. TRPL spectra were acquired using a time-resolved single photon-counting set-up (FluoTime 300, PicoQuant).

Scanning electron microscopy (SEM). SEM was performed on a FEI Sirion XL30 microscopy with a field emission electron source.

Glow Discharge Optical Emission Spectrometer (GDOES). The composition and the depth profile of inorganic perovskite films were analyzed using GDOES technology. The samples were prepared by spun perovskite precursor solution on a clean glass substrate. The GDOES was performed at room using a Horiba GD-Profiler-2 equipped with a differential interferometry profiling system temperature.

RESULTS AND DISSCUSSION

Tin-lead alloyed perovskites with various Sn:Pb ratios were prepared by spin-coating from stoichiometric solutions in DMF/DMSO mixed solvents, and subsequently annealed as described in the experimental section. To explore the effect of Sn incorporation on the bandgap tunability, UV-vis absorption of the films with a range of compositions (Sn molar ratio in tin-lead compounds) was performed. Figure 1a presents optical absorption spectra of the tin-lead films with Sn molar ratio from 0.00 to 1.00. We observe that alloying of Sn and Pb in tin-lead compounds results in bandgap bowing, which tunes the bandgap between 1.78 eV and 1.30 eV (inset in Figure 1a) with increase of Sn ratio from 0.00 to 1.00 except for anomalous bandgap behavior shrinking to 1.28 eV and 1.27 eV observed in two of them, namely 0.75 and 0.88, respectively, similar to that reported in tin-lead based organic-inorganic perovskites.[51] This bowing is possibly due to local distortions of the short range ordering of the tin-lead cations. It is worth mentioning that the ideal bandgap for single-junction photovoltaic devices is between 1.1 eV and 1.4 eV according to the theoretical calculation, [44, 59] beyond the range of most reported all-inorganic perovskites recently. Tin alloying strategy, however, could easily tune the bandgap of the all-inorganic $CsPbI_3$ perovskites from 1.78 eV to the ideal value for photovoltaics. More interestingly, it allows the alloyed perovskite films more stable than the original one, which can be observed simply in the light of transforming time from black phase to yellow phase of the films. Typically, the black $CsPbI_3$ film that obtained at 100 ^oC turned to yellow in seconds when it exposed to ambient atmosphere and based on this background, the absorption spectra of $CsPbI_3$ shown in Figure 1a was measured in a nitrogen-filled glovebox, which is quite different from that of obtained in air (Figure S1). With the incorporation of Sn, the color of the film with 0.25 molar Sn is able to remain unchanged for several minutes in air. Notably, when the Sn molar ration increases to 0.3, the perovskite film could be kept in air for several hours without striking change and its' optical wavelength extend to infrared range. Based on a promising bandgap, air stability (in terms of not discoloring rapidly), and tin % below 50%, which has been shown to be important for oxidation stability,[60] this tin-lead alloyed strategy is therefore promising for efficient and stable photovoltaic devices.

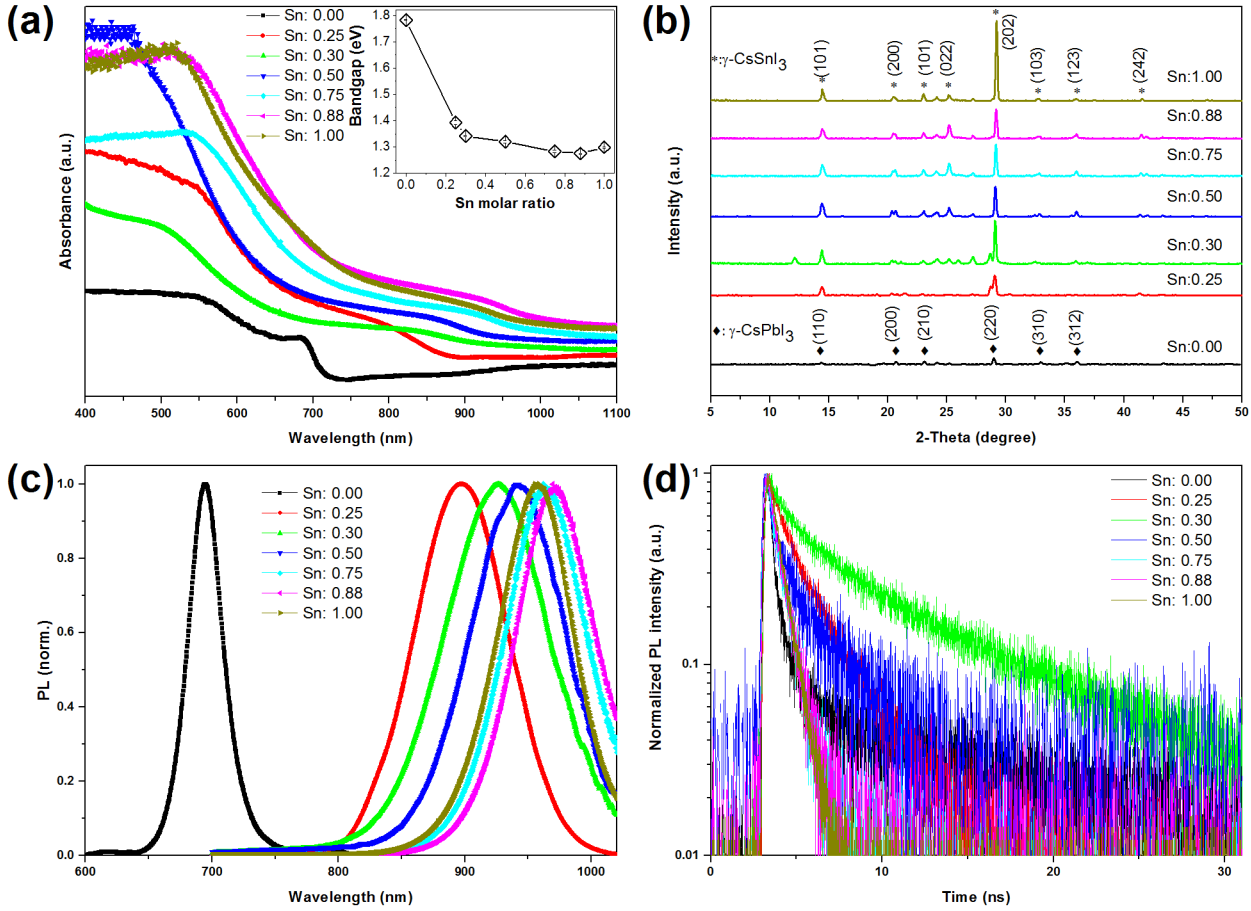

Figure 1. (a) UV-Vis absorption spectra, inset shows the corresponding bandgap (b) XRD patterns, (c) steady-state PL spectra and (d) time-resolved PL curves of tin-lead alloyed perovskite thin films with different Sn molar ratio ranging from 0.00 to 1.00.

To identify the effect of Sn incorporation on the lattice structure of the perovskites, we performed the x-ray diffraction measurements (XRD) at room temperature in ambient condition. Figure 1b shows x-ray diffraction (XRD) patterns of tin-lead compounds for Sn molar ratio ranging from 0.00 to 1.00. For the film without Sn incorporation and with 0.25 molar ration of Sn, which are found to discolor in seconds and in minutes in air, respectively, we seal the samples using Kapton tapes [61] in the glovebox to minimize exposure to air and in fact, the XRD patterns of these two samples are quite different from the results without sealing (Figure S2). As shown in Figure 1a, the sealed film without Sn content exhibits the characteristic peaks at 14.37°, 20.69°,23.01°, 29.02°, 32.87 °, and 36.02 ° and by carefully checking, these peaks can be assigned to the (110), (200), (210), (220), (310) and (312) planes of orthorhombic γ-$CsPbI_3$ structure [31, 62-65] while the XRD patterns of unsealed $CsPbI_3$ sample can be indexed to the non-perovskite orthorhombic δ-$CsPbI_3$ structure (Figure S2) due to discoloring during the measurement.[26, 41] Notably, although the $CsPbI_3$ sample which is obtained at 100 °C pose large bandgap of 1.78 eV, the black appearance and even very close XRD peaks to that obtained at 330 °C, it is actually corresponds to orthorhombic γ-$CsPbI_3$ rather than cubic α-CsPbI3 phase incorrectly as most of the previously reported XRD patterns. [63, 64] For the film with 100% Sn, we index the diffraction peaks at 14.44°, 23.01 ° , 25.16 ° and 29.20 ° to the (110), (120), (202) and (220) planes of the black orthorhombic (B-γ) CsSnI3 perovskite.[46] The XRD patterns in the as-prepared thin films with Sn content between these two end members indicate either single-phase tin-lead alloys or the mixed phase of Sn- and Pb-based perovskites. Regardless the concrete phase, it has been found that the XRD patterns of the unsealed Sn-Pb alloyed perovskites that Sn content are larger than 0.30 retain to be identical between repeated measurements, suggesting that incorporation of Sn in Pb-based perovskite substantially improves the stability of photoactive black phase at room temperature as that of reported FA^+ or metal cation incorporation. [36, 66, 67]Note that the film with 0.30 Sn in molar ratio exhibits very similar XRD patterns to that in γ-$CsPbI_3$ and B-γ $CsSnI_3$ perovskites, accompanied by some new reflection peaks at 12.12 °, 21.16° and 28.68° which differ from any phases of $CsSnI_3$ and $CsPbI_3$ and cannot be indexed to any diffraction peaks of the possible undissolved source materials, namely PbI_2, CsI, SnF_2 or SnI_2/SnI_4,[34]. The result suggests that the crystal structure might be in the following possible forms: black orthorhombic (B-γ) $CsSnI_3$; a mixture of black orthorhombic (B-γ) $CsSnI_3$ and γ-$CsPbI_3$; or a new tin-lead alloyed structure or its mixture (as discussed later).

To gain more insight about the Sn incorporation effect on the optoelectronic properties of inorganic halide perovskite films, we carried out steady-state and time-resolved photoluminescence (TRPL) measurements of tin-lead

alloyed perovskite onto glass substrates, which are shown in Figure 1c and Figure 1d, respectively. As shown in Figure 1c, for every individual composition of the tin-lead films, sharp PL peaks are observed and with the increase of Sn molar ratio in tin-lead alloys, corresponding PL peaks exhibited a redshift step by step except that the emission peaks with Sn ratio of 0.75 and 0.88 are beyond the end member, namely $CsSnI_3$, toward to redshift, in good agreement with absorption onset (Figure 1a). The single PL peak change, continuous absorption onset and corresponding XRD peaks (Figure 1b) strongly suggest that we can rule out the possibility of single B-γ $CsSnI_3$ or its mixture with γ-$CsPbI_3$ perovskites in the films with Sn ratio between two end members and confirm that these products are in new tin-lead crystal structure, i.e. tin-lead alloyed perovskites with single-phase. It is worth mentioning that the PL spectrum of $CsPbI_3$ film, which was measured in a pumping container against discoloring, exhibits band edge emission at ~696 nm, corresponding to a bandgap of 1.78 eV. This result is consistent with the absorption shown in Figure 1 and in good agreement with that of the most recently reported γ-$CsPbI_3$ by Hu et al. [63] Figure 1d shows the TRPL spectra of these tin-lead perovskite films with different Sn molar ratio prepared on glass substrates, and corresponding parameters fitted with biexponential function are given in Table S1, in which two dynamics, a fast decay component τ_1 and slow decay part τ_2 are mainly attributed to bimolecular recombination of photogenerated free carriers and trap-assisted recombination,[68-70] respectively. The pristine film without Sn introduce, $CsPbI_3$, and the films with Sn proportion larger than 50% present negligible slow components and the dynamics of them can be traced to exponential function, indicting low trap density in these films. Notably, the calculated τ_2 of $CsSn_{0.25}Pb_{0.75}I_3$ and $CsSn_{0.30}Pb_{0.70}I_3$ films are 2.88 and 7.65 ns, and the average lifetime of these films are evaluated to be 1.28 and 3.90 ns, respectively. The results might be associated with the trap-assisted recombination, in which an electron falls into a "trap", an energy level within the bandgap caused by the presence of the foreign Sn and either occurs in a second-step falling into an empty in the valence band (Sn molar ratio <50%) to complete the recombination process or directly annihilates in over-formed Sn vacancies (Sn molar ratio >50%).

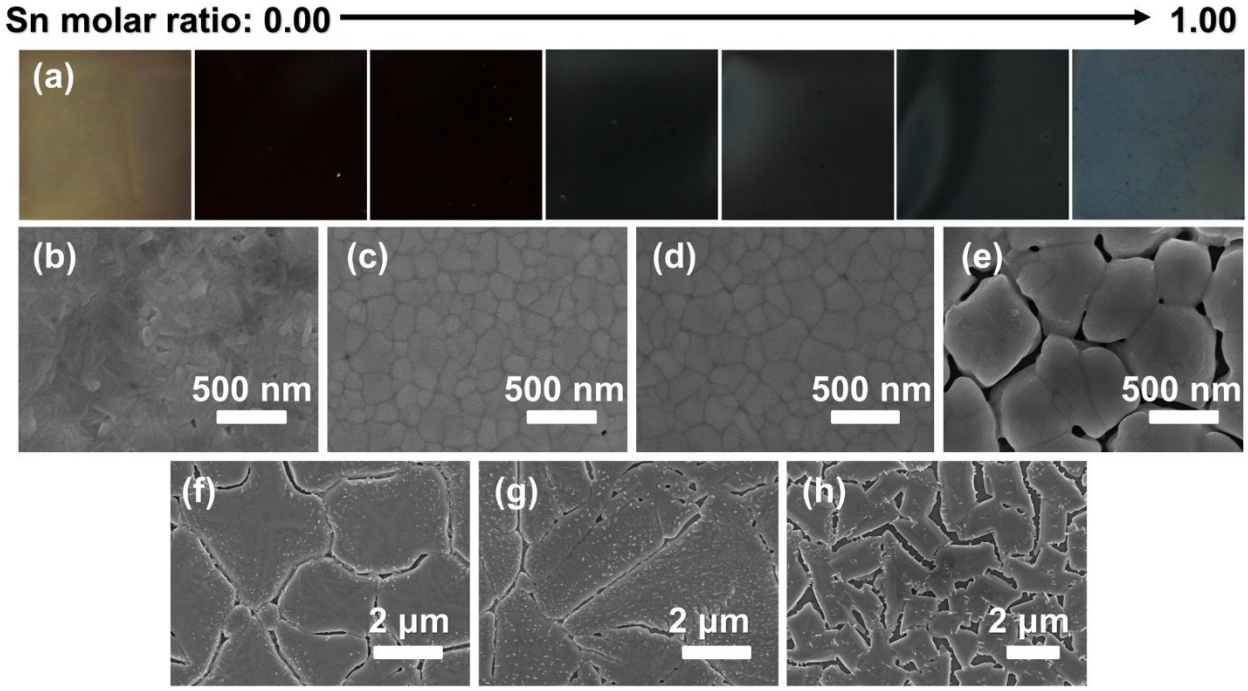

Figure 2. (a) Optical images and top-view of SEM images of tin-lead alloyed thin films with Sn molar ratio of (b)0.00, (c)0.25, (d) 0.30, (e) 0.50, (f) 0.75, (g) 0.88 and (h) 1.00 .

To investigated the effect of the Sn on the change of morphologies, which are prepared using a precursor-phase anti-solvent immersion (PAI) route, [49,51] optical and top-view of scanning electron microscopy (SEM) images of post-annealed tin-lead alloyed films were performed (Figure 2a and Figure 2b~h). From SEM images, we found that the Sn fraction in the precursor source has a crucial influence on the apparent grain size. The pristine $CsPbI_3$ films without Sn incorporation exhibits small crystal domain size about ~200 nm (Figure 2b). As Sn fraction increase from 0.25 to 1.00, the average domain size increase from ~300 nm to several micrometers (Figure 2c~h). However, large nanoscale domains in the films with higher Sn fraction are accompanied by a significant amount of pinhole formation (Figure 2e~h), which might result in a detrimental effect on the performance of devices. In contrast, the films with Sn ratio of 0.25 and 0.30, especially 0.30, displays smoother surface and good coverage with few pinholes (Figure 2c, d). The corresponding color (Figure 2a) of the tin-lead films gradually changed from orange to deep black as the Sn fraction increase from 0.00 to 0.30, whereas further increase Sn fraction, it gradually turned from dark to slight greyish white. It should be noted that the decent black color, uniform and densely coverage surface has been obtained in

the film with Sn fraction of 0.30 (Figure 2c), which would play an important role in the photoelectrical performance of perovskite devices.

To evaluate the feasibility of the tin-lead alloyed absorber in photovoltaic devices, we fabricated inverted planar perovskite solar cells with a structure ITO/Poly(3,4-ethylenedioxythiophene) poly(styrenesulfonate) (PEDOT:PSS)/perovskite/Phenyl-C61-butyric acid methyl ester (PCBM)/bathcuproine (BCP)/Ag as shown in Figure 3a. Figure 3b shows cross-sectional SEM image of a typical devices based on tin-lead thin films with Sn ratio of 0.3, in which all layers are obviously observed corresponding to schematic structure layer by layer and the perovskite absorber shows good crystallinity with ~300 nm in thickness. The photocurrent density-voltage (J-V) curves as a function of the molar ratio of Sn in the tin-lead alloyed perovskite solar cells are shown in Figure 3c, and corresponding photovoltaic parameters are given in Table 1. As shown in Figure 3c, the pure Pb based perovskite solar cell exhibits the highest open circuit voltage (V_{oc}) of ~0.67 V but shows a very low short circuit current density (J_{sc}) of 1.8 mA cm^{-2}, thus leading to a low PCE of 0.61%. In contrast, the lowest V_{oc} of 0.10 V, a J_{sc} of 4.07 mA cm^{-2} corresponding to a PCE of ~0.15% in the pure Sn based perovskite solar cell. Substituting Pb with Sn partially, the V_{oc} varies between these two endpoints which can be attributed to the variation of the decreasing bandgap of the tin-lead absorbers with increase of Sn proportion. In stark contrast to V_{oc}, the tendency of J_{sc}, Fill factor (FF) and PCE are ascend at first and then descend at last as Sn percentage increases. We achieved the highest PCE up to 9.41% with a J_{sc} of 20.96 mA cm^{-2}, FF of 70.12% and V_{oc} of 0.64 V, using the $CsSn_{0.3}Pb_{0.7}I_3$ perovskite film as an active layer in solar cell. This impressive PCE mainly determined by the enhanced J_{sc} and decent FF, which possibly come from the nature of low bandgap (~1.34 eV), long lifetime and the densely coverage of the $CsSn_{0.3}Pb_{0.7}I_3$ perovskite film.

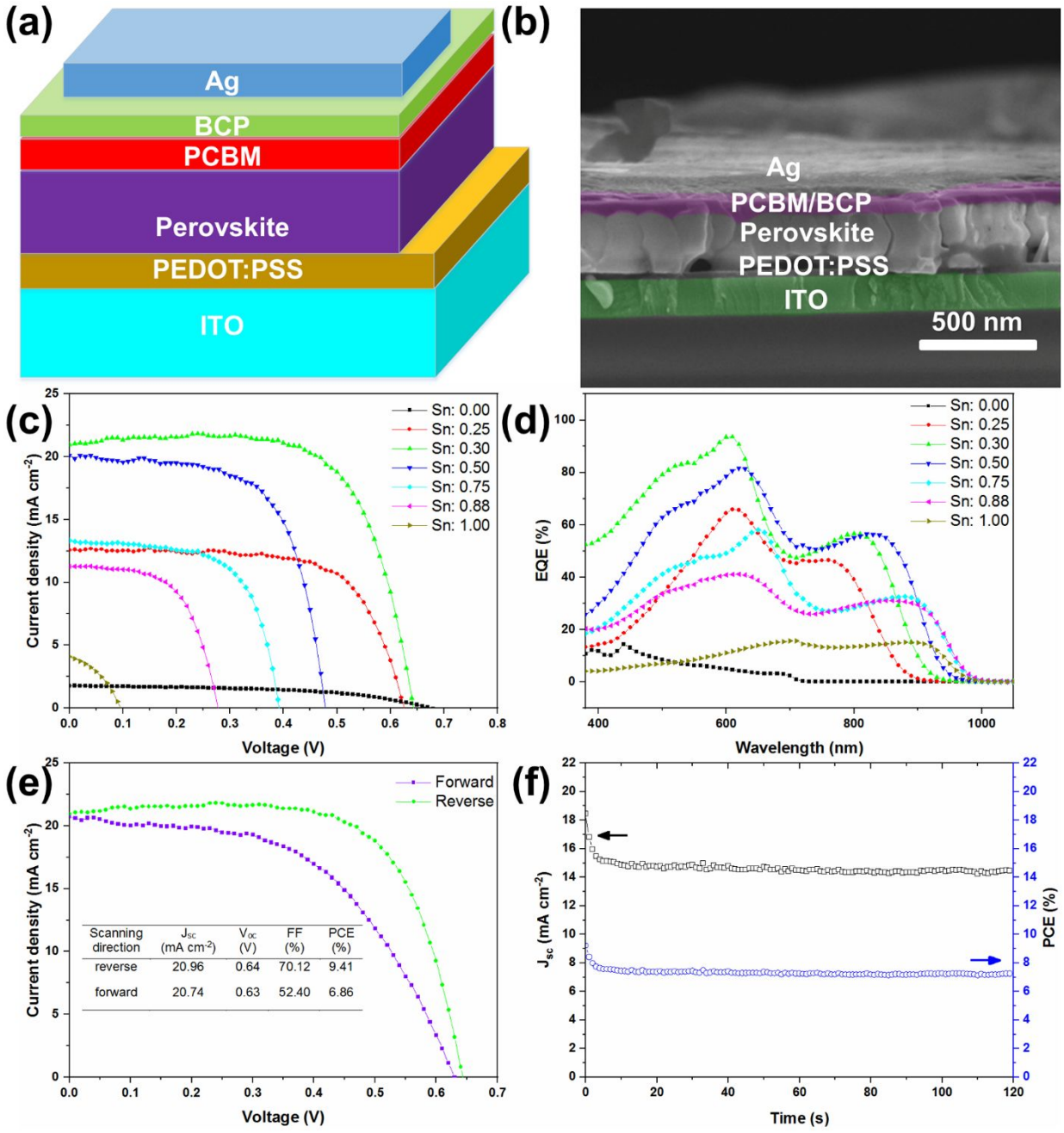

Figure 3. (a) Schematic structure, (b) typical cross-sectional SEM images, (c) photocurrent density-voltage curves (J-V curves) and (d) EQE spectra of tin-lead based perovskite solar cells with Sn molar ratio ranging from 0.00 to 1.00; (e) the J-V curves with forward scanning and reverse scanning and (f) stabilized current density and PCE of the best performing full-structured perovskite solar cells.

Figure 3d shows the external quantum efficiency (EQE) spectra of tin-lead alloyed perovskite solar cells. Obviously, EQE onset wavelength of the tin-lead perovskite solar cells shows a gradual redshift tendency with the increase of the Sn content in tin-lead alloys with an exception of $CsSnI_3$, in good agreement with the UV-vis absorption and PL spectra (Figure 1a, c). For the best performing devices based on $CsSn_{0.3}Pb_{0.7}I_3$ perovskite film, the EQE in the peak larger than 90% has been obtained, superior to that of most reported all-inorganic perovskite solar cells. To check the reliability of the champion solar cell, the J-V scans with forward and reverse direction and stabilized power output (SPO) at maximum power point were measured under continuous illumination of AM1.5G (Figure 3e, f). We note that $CsSn_{0.3}Pb_{0.7}I_3$ based full-structured perovskite solar cell presents a PCE of 9.41% with reverse scanning while has only a PCE of 6.86% (table inset in Figure 3e). As shown in Figure 3f, the steady-state current density dropped quickly at first 15 s and gradually stabled at 14.6 mA cm^{-2}, which induced a similar tendency in steady-state PCE decreasing from 9.22% to 7.23%. It should be noted that $CsSn_{0.3}Pb_{0.7}I_3$ based perovskite solar cells in this device configuration

exhibit pronounced hysteresis in the J-V scanning measurements with a hysteresis index [71] about 21.58%. It is now understood that hysteresis in perovskite solar cells is likely related to both the presence of mobile ionic defects and their interaction with the p- and n- type interfaces.[72] Snaith et al. demonstrated the specific device architecture affects the severity of this behavior in perovskite solar cells.[73] Others[74, 75] have also pointed out the PEDOT:PSS in the inverted planar structure solar cells may induce stability issues due to the poor chemical stability of PEDOT:PSS: the reaction at the interface between the active layer and PEDOT:PSS has been demonstrated to be a major cause of device failure in inverted devices.[76, 77] We thus hypothesize that PEDOT:PSS might be a non-ideal contact here and we found that ,remarkably, we could in fact attain effective and less hysteresis devices by removing the hole transport layer entirely, following the demonstration of effective hole-transport-material-free (HTM-free) Sn-based perovskite solar cells.[46]

Table 1. Key photovoltaic parameters derived from the J-V curves of fully-structured perovskite solar cells in Figure 3c with different Sn molar ration in tin-lead compounds.

Sn molar ratio	J_{sc} (mA cm^{-2})	V_{oc} (V)	FF (%)	PCE (%)
0.00	1.78	0.67	50.88	0.61
0.25	12.58	0.63	67.39	5.34
0.30	20.96	0.64	70.12	9.41
0.50	20.10	0.48	64.44	6.22
0.75	13.34	0.39	64.05	3.33
0.88	11.28	0.28	58.71	1.85
1.00	4.07	0.10	36.53	0.15

Prior to fabricate the HTM-free devices based on the thin films with different Sn molar ratio, which are designated with the stoichiometry ratio in precursor solution, we conduct the X-ray photoelectron spectra (XPS) and ultra-violet photoelectron spectra to identify the atomic composition and electronic structure of the samples. A typical survey spectrum of the perovskite film with Sn ratio of 0.3 (Figure 4a) identify the presence of both Sn and Pb, compared to the only metal Sn in $CsSnI_3$ and Pb in $CsPbI_3$ (Figure S3). High-resolution XPS spectra of the Cs 3d, Sn 3d, Pb 4f and I 3d were performed, which can distinguish the oxidation state of the corresponding elements (Figure 4c~f). The characteristic peaks of Sn 3d observed at 486.2 eV and 494.6 eV with a peak splitting of 8.4 eV which is assigned to Sn^{2+} 3d5/2 and 3d3/2, respectively, and distinct from that of Sn^{4+} and Sn^0 suggesting no oxidation or disproportionation has taken place here. The narrow doublet peaks of Pb 4f appear at 137.8 eV and 142.6 eV with a separation of 4.8 eV, indicating the Pb is also in the Pb^{2+} state as expected. The chemical composition from XPS spectra shows that the atomic ratios of the elements of Sn and Pb in the present film is about 2.95 and 7.14, respectively, which are very close to the 3:7 in the precursor solutions. The elemental distribution was also confirmed by glow discharge optical emission spectroscopy (GDOES) analysis, which probes the chemical composition as a function of sputtering time (film depth) (Figure S4). As shown in Figure S4, the atomic ratio of Sn and Pb from surface to depth etched is consistent with the XPS measurement suggesting Sn and Pb coexist and the distribution of them is fairly homogeneous through the cross-section layer of the film. Figure 4b shows the typical UPS of the film with Sn ratio of 0.30, in which the valence band maximum (VBM) is determined to be 5.44 eV and corresponding conduction band minimum (CBM) was estimated to be 4.10 eV based on the optical bandgap.

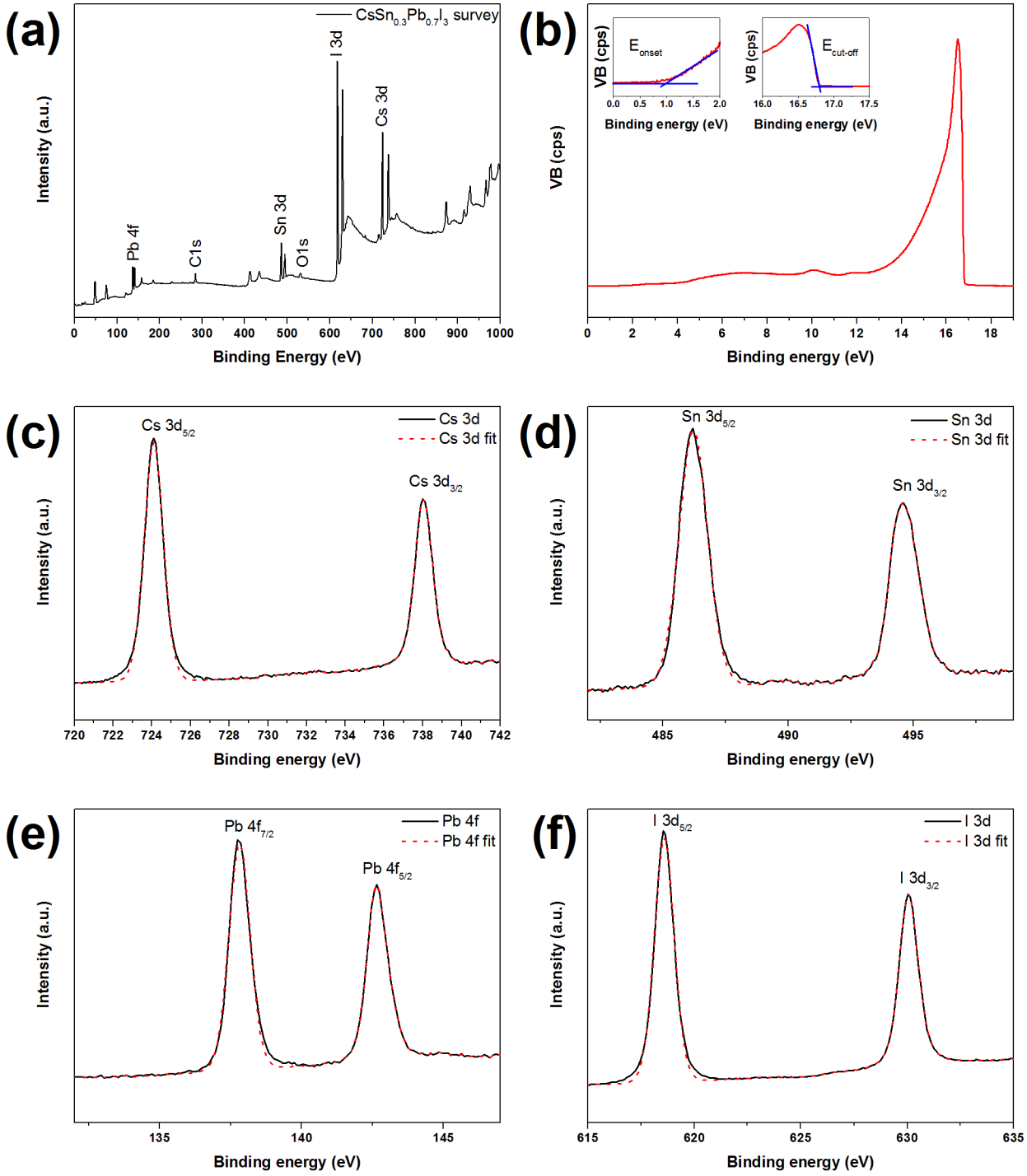

Figure 4. (a) XPS survey spectrum (b) UPS spectrum, and high resolution XPS core level for (c) Cs 3d, (d) Sn 3d, (e) Pb 4f, and (f) I 3d of the tin-lead perovskite film with Sn molar ratio of 0.30 (dashed red lines in (c)~(f) correspond to curve fitting with CasaXPS).

The HTM-free devices are fabricated with the structure of ITO/perovskite/PCBM/BCP/Ag (Figure 5a) by removing the PEDOT:PSS hole transport material in the inverted full structure (Figure 3a). The typical energy-level band alignment of the HTM free perovskite solar cells based on the film with Sn of 0.30 are shown in Figure 5b. This energy level alignment between $CsSn_{0.3}Pb_{0.7}I_3$ and PCBM should facilitate electron extraction and block holes. Corresponding cross-sectional SEM image are shown in Figure 5c, in which all functional films are well layered and the thickness of the $CsSn_{0.3}Pb_{0.7}I_3$ perovskites is estimated to be ~300 nm, in good agreement with that of full-inverted structure devices. We tested different two end member films, namely $CsPbI_3$ and $CsSnI_3$, and other Sn-Pb ratios in this structure (Figure S5 and Figure S6). As shown in Figure S5 and Table S2, HTM-free devices with $CsPbI_3$ and $CsSnI_3$

are almost under the short-circuit condition and in fact, with Sn fraction above 40%, most devices are in the same situation of short-circuit (Figure S6) – this result is consistent with literature suggesting that tin-lead alloyed materials become exponentially more susceptible to heavy doping via oxidation as Sn content increases; this heavy doping likely creates shunting paths through the perovskite, which would be more of an issue when there no hole-selective contact present,[60] whereas tin-lead films with Sn ratio ranging from 0.10 to 0.35 are valid in the HTM-free structure (Figure S6, key parameters are summarized in Table S3). The PCE of these devices increase gradually with the increase of the Sn molar ratio till the optimal value has been achieved in the films with Sn ratio of 0.30, and then drop down gradually with the increasing Sn. We associate the result of the validity of the devices based on the lower Sn incorporation (typical Sn ratio <50%) with the intermediate energy level formed between the VBM and CBM coming from the foreign atom, which will facilitate the carrier transport as described in the TRPL when the HTM is absent in the devices, but the mechanism is not fully understand yet and it would be further investigated in our future work. The J-V characteristics of the HTM-free solar cells based on $CsSn_{0.3}Pb_{0.7}I_3$ was carried out under the same condition as that of full-structured solar cells (Figure 5c). Compared with the full-structured devices, an even higher J_{sc} of 21.97 mA cm^{-2} is achieved, and an impressive PCE of 7.60% has been obtained in spite of slightly decreasing V_{oc} and FF of 0.60 V and 57.65%. Moreover, the J-V curves of devices measured under forward and reverse scanning with different scan rates show less hysteresis with a small hysteresis index only 6.72% than the full-structured devices, which is further confirmed with J-V bi-directional scanning with different sweep rate as shown in Figure S7 (corresponding parameters summarized in Table S4). The EQE spectrum with an integrated current density and SPO of the HTM-free device based on $CsSn_{0.3}Pb_{0.7}I_3$ are presented in Figure 5d and Figure 5e, respectively. As shown in Figure 5d, almost all of the EQE values with little fluctuation are larger than 82% in the wavelength between 420 nm to 600 nm, where it shows a linear-like change in the full-structured devices (Figure 3d). This can be ascribed to less parasitic absorption in the absent PEDOT:PSS layer and is consistent with higher current density in the HTM-free devices. The EQE also shows a broad response with wavelength onset up to 925 nm, indicating a bandgap of ~1.34 eV for this film, which is consistent with the UV-Vis absorption (Figure 1a) and that in the full-structured device (Figure 3d). The photocurrent density integrated from EQE spectrum with the AM1.5G solar photo flux are found to be consistent with the J_{sc} extracted from J-V curves as shown in Figure 5c. Importantly, instead of the dramatic decrease of PCE at steady state seen with the full-structured cells, the power output stabilizes at ~7.31% with the HTM-free devices during maximum power point tracking as shown in Figure 5e. This stabilized PCE is very close to that extracted from the J-V plot and notably, even without HTM layer, it is in fact superior to that in the full-structured devices. More importantly, to the best of our knowledge, this is the highest efficiency to date for an inorganic perovskite solar cell with the bandgap below 1.40 eV, especially for the HTM-free inorganic perovskite devices.

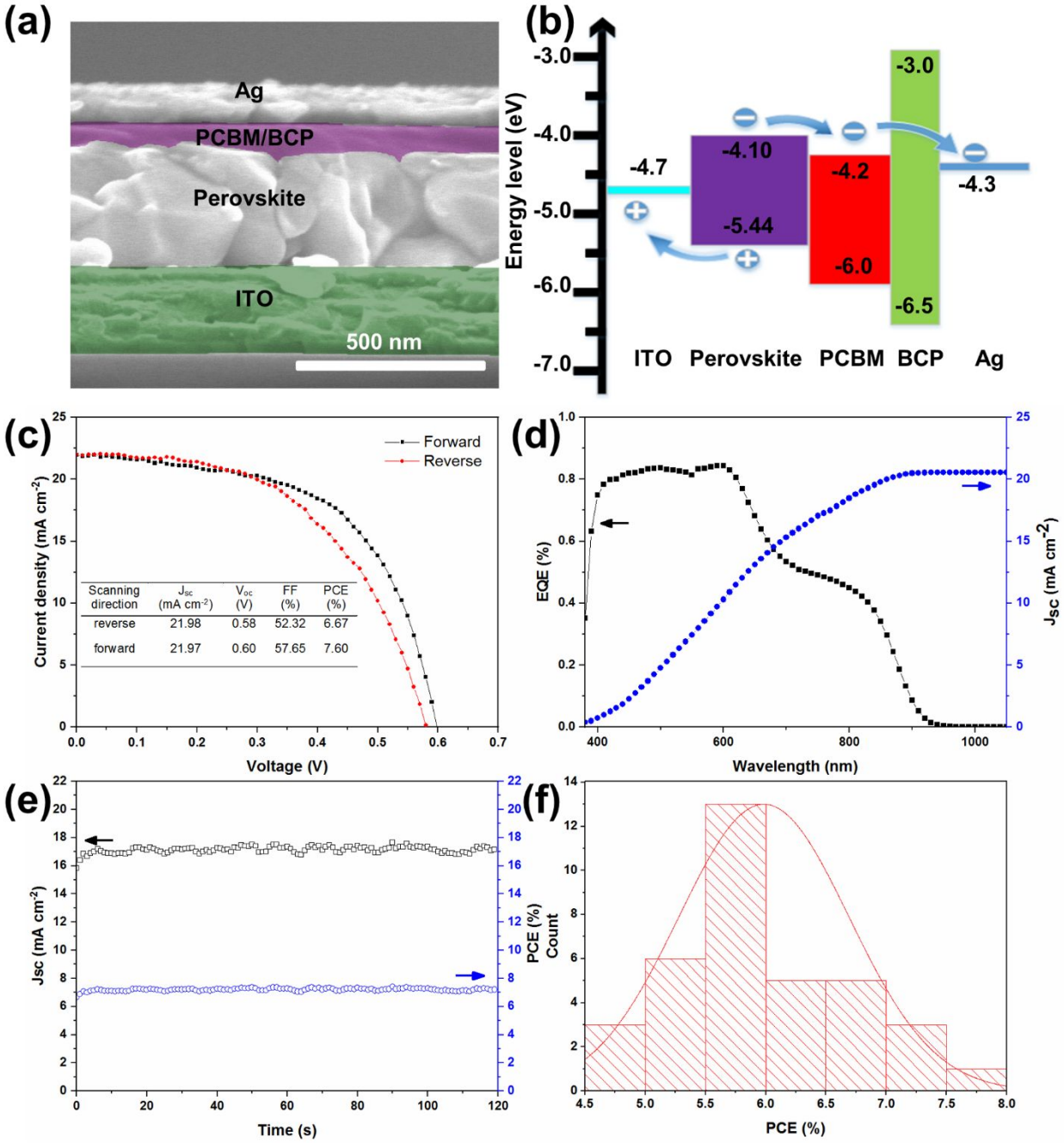

Figure 5. (a)Typical cross-sectional SEM image, (b) energy level diagram, (c) J-V curves, (d) EQE and integrated current density, (e) stabilized power output at maximum power tracking point of the reported HTM-free perovskite solar cells based on $CsSn_{0.3}Pb_{0.7}I_3$ film, (f)Statistical histogram distribution of PCEs extracted from 36 individual $CsSn_{0.3}Pb_{0.7}I_3$ based HTM-free perovskite solar cells

To test the reproducibility of the HTM-free devices, we measured J-V curves of 36 individual $CsSn_{0.3}Pb_{0.7}I_3$ based PEDOT-free perovskite solar cells. Figure 5f shows the histograms of the J-V scan PCEs of these cells. We note that the distribution of the PCEs lie in a range from 4.87% to 7.60% with an average PCE of 5.98%±0.70%, implying reasonable reproducibility of the tin-lead alloyed solar cells.

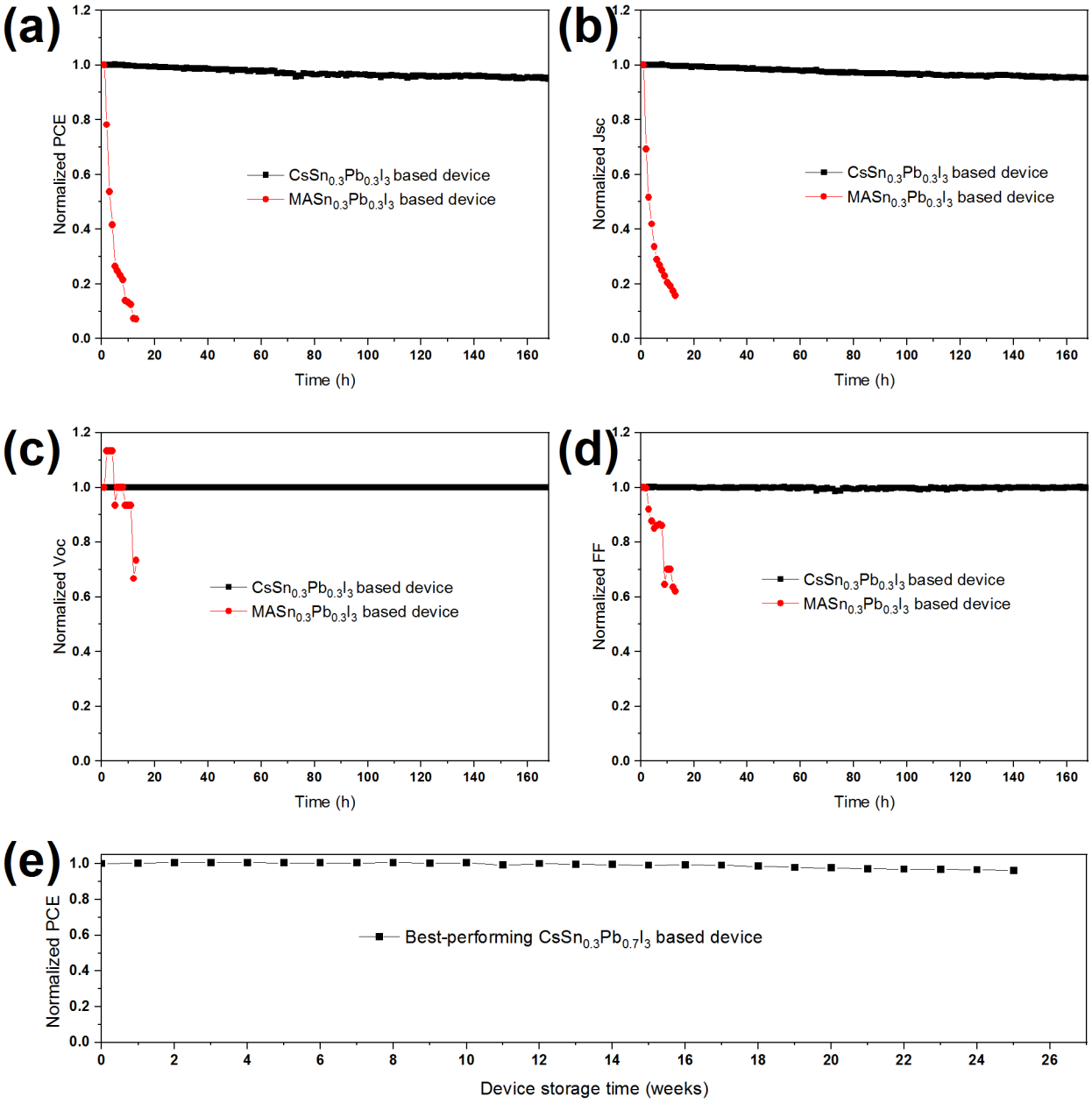

Figure 6. Normalized photovoltaic performance of (a) PCE, (b) J_{sc}, (c) V_{oc} and (d) FF as a function aging time of the perovskite solar cells based on $CsSn_{0.3}Pb_{0.7}I_3$ and $MASn_{0.3}Pb_{0.7}I_3$ without encapsulation under one-sun continuous illumination in glovebox and (e) Photostability of the $CsSn_{0.3}Pb_{0.7}I_3$ based perovskite solar cells without encapsulation as a function of storage time in glovebox measured for every week.

Finally, we probed the photostability of HTM-free perovskite solar cells based on inorganic $CsSn_{0.3}Pb_{0.7}I_3$ films under continuous one-sun illumination in a nitrogen-filled glovebox. For comparison, we fabricated organic-inorganic counterparts- $MASn_{0.3}Pb_{0.7}I_3$ based devices as the controlled samples. Figure 6 shows the normalized photovoltaic parameters as a function of the illuminated time of the devices for more than 168 h, in which measurements were automatically performed every hour by Keithley 2400 via a computer-controlled program. During the measurements, $MASn_{0.3}Pb_{0.7}I_3$-based device showed an improvement in V_{oc} at the beginning of the measurement, the device performance dropped quickly with rapid decline in J_{sc} and FF and after 8 h light soaking, the PCE of the device retains under 8% of original efficiency. In contrast, the FF of $CsSn_{0.3}Pb_{0.7}I_3$-based device fluctuated between 98.45% and 100.17% of the initial value, and J_{sc} exhibited slight increase for the first 8 h and then followed slow drop at the rest of the time, whereas V_{oc} remained unchanged with a constant value of 0.66 V. Eventually, the overall PCE of the device exhibited no significant change and remained 94.86% of that from the start point after 168 h continuous illumination, suggesting a negligible light soaking effect which might ascribe to the large ion migration barrier of the inorganic perovskite. [23, 78] These results indicate that $CsSn_{0.3}Pb_{0.7}I_3$-based device poses good photostability which is a very important for practical application of the solar cells. We further investigated long term stability of the all-

inorganic $CsSn_{0.3}Pb_{0.7}I_3$-based device by measuring best-performing device after every 7 days (Figure 6e) which was stored in an opaque container in the glovebox. The corresponding PCE of the device remains more than 97% of the fresh one even after almost 6 months. Besides the stability in the glovebox, we also examined the air stability of $CsSn_{0.3}Pb_{0.7}I_3$-based device compared to that of most recently reported inorganic $CsPbI_2Br$ based perovskite solar cells, which are considered to the be the state-of-the-art all-inorganic photovoltaic (PV) devices with good stability.[28, 29, 39, 79, 80] The stability tests of are carried out in the ambient atmosphere by measuring the PCE (extracted from J-V curves) for every 2 hours (Figure S8). We observed that $CsPbI_2Br$ based device display a nearly linear decrease in PCE and quenched after stored for 22 hours in air. Notably, the PCE of $CsSn_{0.3}Pb_{0.7}I_3$ based devices show no obvious loss at the first 4 hours exposing in air and then slight loss finishing at 87.0% of the initial value at the end of the period, indicting excellent moisture resistance of our simplified tin-lead alloyed device, which might come from the enhanced phase stability by incorporation of Sn.

CONCLUSIONS

In summary, we have demonstrated that partially substituting Pb with Sn in all-inorganic perovskites is a promising strategy to stabilize the photoactive black phase at low temperature and attain efficient and stable solar cells with ideal bandgap. With alloyed $CsSn_{0.3}Pb_{0.7}I_3$ perovskite, we are able to fabricate functional solar cells both with and without a PEDOT:PSS hole transport material. These devices showed promising PCEs of 9.41% and 7.60% (stabilized PCE of 7.23% and 7.31%) respectively, making these devices the most efficient low bandgap all-inorganic perovskite solar cells reported to date. Moreover, we found that the simplified HTM-free $CsSn_{0.3}Pb_{0.7}I_3$ based devices exhibit good photostability with negligible light soaking and long-term stability in the glovebox. The good moisture resistance of unencapsulated devices in air is also presented. There is still much room for improvement in the performance of $CsSn_{0.3}Pb_{0.7}I_3$ based solar cells and the incorporation of Sn into inorganic perovskites opens up new possibilities for attaining extremely stable and highly efficient perovskite solar cells in the future.

ASSOCIATED CONTENT

Supporting Information

The Supporting Information is available free of charge at:

Additional data for UV-Vis absorption, XRD, TRPL, XPS, GDOES, J-V and air stability characterization.

AUTHOR INFORMATION

Corresponding Author

*Email: giles.eperon@nrel.gov

*Email: dginger@uw.edu

Present Addresses

§National Renewable Energy Laboratory (NREL), Golden, Colorado 80401, United States

Author Contributions

#These authors contributed equally.

Notes

The authors declare no competing financial interest.

ACKNOWLEDGMENT

This work was supported by Zhejiang Provincial Nature Science Foundation of China (Grant No. LY18F040008), Natural Science Foundation of Ningbo Municipal Government of China (Grant No. 2016A610108), Foundation of Department of Education of Zhejiang Province (Grant No. Y201533502), the DOE BES DE-SC0013957 and National Natural Science Foundation of China (NSFC, Grant No. 11401328). Part of this work was conducted at the Molecular Analysis Facility, a National Nanotechnology Coordinated Infrastructure site at the University of Washington, which is supported in part by the National Science Foundation (Grant ECC-1542101), the University of Washington, the Molecular Engineering & Sciences Institute, the Clean Energy Institute, and the National Institutes of Health. We thank Mark Ziffer for assistance with EQE measurements and photoluminescence characterization.

REFERENCES

1. Hao, F.; Stoumpos, C. C.; Cao, D. H.; Chang, R. P. H.; Kanatzidis, M. G., Lead-free solid-state organic–inorganic halide perovskite solar cells. *Nature Photonics* **2014,** 8, 489-494.

2. Stranks, S. D.; Eperon, G. E.; Grancini, G.; Menelaou, C.; Alcocer, M. J.; Leijtens, T.; Herz, L. M.; Petrozza, A.; Snaith, H. J., Electron-hole diffusion lengths exceeding 1 micrometer in an organometal trihalide perovskite absorber. *Science* **2013,** 342, 341-344.

3. Dong, Q.; Fang, Y.; Shao, Y.; Mulligan, P.; Qiu, J.; Cao, L.; Huang, J., Solar cells. Electron-hole diffusion lengths > 175 mum in solution-grown $CH_3NH_3PbI_3$ single crystals. *Science* **2015,** 347, 967-970.

4. Bi, D.; Yi, C.; Luo, J.; Décoppet, J.-D.; Zhang, F.; Zakeeruddin, Shaik M.; Li, X.; Hagfeldt, A.; Grätzel, M., Polymer-templated nucleation and crystal growth of perovskite films for solar cells with efficiency greater than 21%. *Nat Energy* **2016,** 1, 16142-16146.

5. Kojima, A.; Teshima, K.; Shirai, Y.; Miyasaka, T., Organometal halide perovskites as visible-light sensitizers for photovoltaic cells. *J Am Chem Soc* **2009,** 131, 6050-6051.

6. Kim, H. S.; Lee, C. R.; Im, J. H.; Lee, K. B.; Moehl, T.; Marchioro, A.; Moon, S. J.; Humphry-Baker, R.; Yum, J. H.; Moser, J. E.; Gratzel, M.; Park, N. G., Lead iodide perovskite sensitized all-solid-state submicron thin film mesoscopic solar cell with efficiency exceeding 9%. *Sci Rep* **2012,** 2, 591-597.

7. Yang, W. S.; Noh, J. H.; Jeon, N. J.; Kim, Y. C.; Ryu, S.; Seo, J.; Seok, S. I., SOLAR CELLS. High-performance photovoltaic perovskite layers fabricated through intramolecular exchange. *Science* **2015,** 348, 1234-1237.

8. Yu, Z. S.; Leilaeioun, M.; Holman, Z., Selecting tandem partners for silicon solar cells. *Nat Energy* **2016,** 1, 16137-16140.
9. Dong, Y.; Li, W.; Zhang, X.; Xu, Q.; Liu, Q.; Li, C.; Bo, Z., Highly Efficient Planar Perovskite Solar Cells Via Interfacial Modification with Fullerene Derivatives. *Small* **2016,** 12, 1098-1104.
10. Best Research-Cell Efficiency Chart, https://www.nrel.gov/pv/cell-efficiency.html, accessed March 11,2020.
11. Correa-Baena, J. P.; Saliba, M.; Buonassisi, T.; Gratzel, M.; Abate, A.; Tress, W.; Hagfeldt, A., Promises and challenges of perovskite solar cells. *Science* **2017,** 358, 739-744.
12. Qiu, L.; Ono, L. K.; Qi, Y., Advances and challenges to the commercialization of organic–inorganic halide perovskite solar cell technology. *Materials Today Energy* **2018,** 7, 169-189.
13. Conings, B.; Drijkoningen, J.; Gauquelin, N.; Babayigit, A.; D'Haen, J.; D'Olieslaeger, L.; Ethirajan, A.; Verbeeck, J.; Manca, J.; Mosconi, E.; Angelis, F. D.; Boyen, H.-G., Intrinsic Thermal Instability of Methylammonium Lead Trihalide Perovskite. *Adv Energy Mater* **2015,** 5, 1500477-1500484.
14. Salado, M.; Calio, L.; Berger, R.; Kazim, S.; Ahmad, S., Influence of the mixed organic cation ratio in lead iodide based perovskite on the performance of solar cells. *Phys Chem Chem Phys* **2016,** 18, 27148-27157.
15. Christians, J. A.; Miranda Herrera, P. A.; Kamat, P. V., Transformation of the excited state and photovoltaic efficiency of $CH_3NH_3PbI_3$ perovskite upon controlled exposure to humidified air. *J Am Chem Soc* **2015,** 137, 1530-1538.
16. Binek, A.; Hanusch, F. C.; Docampo, P.; Bein, T., Stabilization of the Trigonal High-Temperature Phase of Formamidinium Lead Iodide. *J Phys Chem Lett* **2015,** 6, 1249-1253.
17. Han, Y.; Meyer, S.; Dkhissi, Y.; Weber, K.; Pringle, J. M.; Bach, U.; Spiccia, L.; Cheng, Y. B., Degradation observations of encapsulated planar $CH_3NH_3PbI_3$ perovskite solar cells at high temperatures and humidity. *J Mater Chem A* **2015,** 3, 8139-8147.
18. Song, Z. N.; Abate, A.; Watthage, S. C.; Liyanage, G. K.; Phillips, A. B.; Steiner, U.; Graetzel, M.; Heben, M. J., Perovskite Solar Cell Stability in Humid Air: Partially Reversible Phase Transitions in the PbI_2-CH_3NH_3I-H_2O System. *Adv Energy Mater* **2016,** 6, 1600846-1600852.
19. Stoumpos, C. C.; Malliakas, C. D.; Kanatzidis, M. G., Semiconducting tin and lead iodide perovskites with organic cations: phase transitions, high mobilities, and near-infrared photoluminescent properties. *Inorg Chem* **2013,** 52, 9019-9038.
20. Zhang, M.; Yun, J. S.; Ma, Q. S.; Zheng, J. H.; Lau, C. F. J.; Deng, X. F.; Kim, J.; Kim, D.; Seidel, J.; Green, M. A.; Huang, S. J.; Ho-Baillie, A. W. Y., High-Efficiency Rubidium-Incorporated Perovskite Solar Cells by Gas Quenching. *Acs Energy Letters* **2017,** 2, 438-444.
21. Jung, Y. K.; Lee, J. H.; Walsh, A.; Soon, A., Influence of Rb/Cs Cation-Exchange on Inorganic Sn Halide Perovskites: From Chemical Structure to Physical Properties. *Chem Mater* **2017,** 29, 3181-3188.
22. Liang, J.; Wang, C.; Wang, Y.; Xu, Z.; Lu, Z.; Ma, Y.; Zhu, H.; Hu, Y.; Xiao, C.; Yi, X.; Zhu, G.; Lv, H.; Ma, L.; Chen, T.; Tie, Z.; Jin, Z.; Liu, J., All-Inorganic Perovskite Solar Cells. *J Am Chem Soc* **2016,** 138, 15829-15832.
23. Wang, P.; Zhang, X.; Zhou, Y.; Jiang, Q.; Ye, Q.; Chu, Z.; Li, X.; Yang, X.; Yin, Z.; You, J., Solvent-controlled growth of inorganic perovskite films in dry environment for efficient and stable solar cells. *Nat Commun* **2018,** 9, 2225-2231.
24. Kulbak, M.; Gupta, S.; Kedem, N.; Levine, I.; Bendikov, T.; Hodes, G.; Cahen, D., Cesium Enhances Long-Term Stability of Lead Bromide Perovskite-Based Solar Cells. *J Phys Chem Lett* **2016,** 7, 167-172.
25. Saliba, M.; Matsui, T.; Seo, J. Y.; Domanski, K.; Correa-Baena, J. P.; Nazeeruddin, M. K.; Zakeeruddin, S. M.; Tress, W.; Abate, A.; Hagfeldt, A.; Gratzel, M., Cesium-containing triple cation perovskite solar cells: improved stability, reproducibility and high efficiency. *Energy Environ Sci* **2016,** 9, 1989-1997.
26. Eperon, G. E.; Paterno, G. M.; Sutton, R. J.; Zampetti, A.; Haghighirad, A. A.; Cacialli, F.; Snaith, H. J., Inorganic caesium lead iodide perovskite solar cells. *J Mater Chem A* **2015,** 3, 19688-19695.
27. Dastidar, S.; Egger, D. A.; Tan, L. Z.; Cromer, S. B.; Dillon, A. D.; Liu, S.; Kronik, L.; Rappe, A. M.; Fafarman, A. T., High Chloride Doping Levels Stabilize the Perovskite Phase of Cesium Lead Iodide. *Nano Lett* **2016,** 16, 3563-3570.
28. Sutton, R. J.; Eperon, G. E.; Miranda, L.; Parrott, E. S.; Kamino, B. A.; Patel, J. B.; Horantner, M. T.; Johnston, M. B.; Haghighirad, A. A.; Moore, D. T.; Snaith, H. J., Bandgap-Tunable Cesium Lead Halide Perovskites with High Thermal Stability for Efficient Solar Cells. *Adv Energy Mater* **2016,** 6, 1502458-1502463.
29. Beal, R. E.; Slotcavage, D. J.; Leijtens, T.; Bowring, A. R.; Belisle, R. A.; Nguyen, W. H.; Burkhard, G. F.; Hoke, E. T.; McGehee, M. D., Cesium Lead Halide Perovskites with Improved Stability for Tandem Solar Cells. *J Phys Chem Lett* **2016,** 7, 746-751.
30. Lin, J.; Lai, M.; Dou, L.; Kley, C. S.; Chen, H.; Peng, F.; Sun, J.; Lu, D.; Hawks, S. A.; Xie, C.; Cui, F.; Alivisatos, A. P.; Limmer, D. T.; Yang, P., Thermochromic halide perovskite solar cells. *Nat Mater* **2018,** 17, 261-267.
31. Steele, J. A.; Jin, H.; Dovgaliuk, I.; Berger, R. F.; Braeckevelt, T.; Yuan, H.; Martin, C.; Solano, E.; Lejaeghere, K.; Rogge, S. M. J.; Notebaert, C.; Vandezande, W.; Janssen, K. P. F.; Goderis, B.; Debroye, E.; Wang, Y. K.; Dong, Y.; Ma, D.; Saidaminov, M.; Tan, H.; Lu, Z.; Dyadkin, V.; Chernyshov, D.; Van Speybroeck, V.; Sargent, E. H.; Hofkens, J.; Roeffaers, M. B. J., Thermal unequilibrium of strained black CsPbI3 thin films. *Science* **2019,** 365, 679-684.
32. Luo, P.; Xia, W.; Zhou, S.; Sun, L.; Cheng, J.; Xu, C.; Lu, Y., Solvent Engineering for Ambient-Air-Processed, Phase-Stable $CsPbI_3$ in Perovskite Solar Cells. *J Phys Chem Lett* **2016,** 7, 3603-3608.
33. Swarnkar, A.; Marshall, A. R.; Sanehira, E. M.; Chernomordik, B. D.; Moore, D. T.; Christians, J. A.; Chakrabarti, T.; Luther, J. M., Quantum dot-induced phase stabilization of alpha-$CsPbI_3$ perovskite for high-efficiency photovoltaics. *Science* **2016,** 354, 92-95.
34. Liu, F.; Ding, C.; Zhang, Y.; Ripolles, T. S.; Kamisaka, T.; Toyoda, T.; Hayase, S.; Minemoto, T.; Yoshino, K.; Dai, S.; Yanagida, M.; Noguchi, H.; Shen, Q., Colloidal Synthesis of Air-Stable Alloyed $CsSn_{1-x}Pb_xI_3$ Perovskite Nanocrystals for Use in Solar Cells. *J Am Chem Soc* **2017,** 139, 16708-16719.
35. Liu, C.; Li, W.; Zhang, C.; Ma, Y.; Fan, J.; Mai, Y., All-Inorganic $CsPbI_2Br$ Perovskite Solar Cells with High Efficiency Exceeding 13%. *J Am Chem Soc* **2018,** 140, 3825-3828.
36. Hu, Y.; Bai, F.; Liu, X.; Ji, Q.; Miao, X.; Qiu, T.; Zhang, S., Bismuth Incorporation Stabilized α-$CsPbI_3$ for Fully Inorganic Perovskite Solar Cells. *ACS Energy Letters* **2017,** 2, 2219-2227.
37. Chang, X.; Li, W.; Zhu, L.; Liu, H.; Geng, H.; Xiang, S.; Liu, J.; Chen, H., Carbon-Based $CsPbBr_3$ Perovskite Solar Cells: All-Ambient Processes and High Thermal Stability. *ACS Appl Mater Interfaces* **2016,** 8, 33649-33655.
38. Liang, J.; Zhao, P.; Wang, C.; Wang, Y.; Hu, Y.; Zhu, G.; Ma, L.; Liu, J.; Jin, Z., $CsPb_{0.9}Sn_{0.1}IBr_2$ Based All-Inorganic Perovskite Solar Cells with Exceptional Efficiency and Stability. *J Am Chem Soc* **2017,** 139, 14009-14012.
39. Bian, H.; Bai, D.; Jin, Z.; Wang, K.; Liang, L.; Wang, H.; Zhang, J.; Wang, Q.; Liu, S., Graded Bandgap $CsPbI_{2+x}Br_{1-x}$ Perovskite Solar Cells with a Stabilized Efficiency of 14.4%. *Joule* **2018,** 2, 1500-1510.
40. Ma, Q. S.; Huang, S. J.; Wen, X. M.; Green, M. A.; Ho-Baillie, A. W. Y., Hole Transport Layer Free Inorganic $CsPbIBr_2$ Perovskite Solar Cell by Dual Source Thermal Evaporation. *Adv Energy Mater* **2016,** 6, 1502202-1502206.
41. Hoffman, J. B.; Schleper, A. L.; Kamat, P. V., Transformation of Sintered $CsPbBr_3$ Nanocrystals to Cubic $CsPbI_3$ and Gradient

$CsPbBr_xI_{3-x}$ through Halide Exchange. *J Am Chem Soc* **2016,** 138, 8603-8611.
42. Frolova, L. A.; Anokhin, D. V.; Piryazev, A. A.; Luchkin, S. Y.; Dremova, N. N.; Stevenson, K. J.; Troshin, P. A., Highly Efficient All-Inorganic Planar Heterojunction Perovskite Solar Cells Produced by Thermal Coevaporation of CsI and PbI_2. *J Phys Chem Lett* **2017,** 8, 67-72.
43. Kulbak, M.; Cahen, D.; Hodes, G., How Important Is the Organic Part of Lead Halide Perovskite Photovoltaic Cells? Efficient $CsPbBr_3$ Cells. *J Phys Chem Lett* **2015,** 6, 2452-2456.
44. Shockley, W.; Queisser, H. J., Detailed Balance Limit of Efficiency of p‐n Junction Solar Cells. *Journal of Applied Physics* **1961,** 32, 510-519.
45. Alharbi, F. H.; Kais, S., Theoretical limits of photovoltaics efficiency and possible improvements by intuitive approaches learned from photosynthesis and quantum coherence. *Renewable & Sustainable Energy Reviews* **2015,** 43, 1073-1089.
46. Marshall, K. P.; Walker, M.; Walton, R. I.; Hatton, R. A., Enhanced stability and efficiency in hole-transport-layer-free $CsSnI_3$ perovskite photovoltaics. *Nat Energy* **2016,** 1, 16178-16186.
47. Zhu, P. C.; Chen, C. L.; Gu, S.; Lin, R. X.; Zhu, J., $CsSnI_3$ Solar Cells via an Evaporation-Assisted Solution Method. *Solar Rrl* **2018,** 2, 1700224-1700228.
48. Liu, B. A.; Long, M. Q.; Cai, M. Q.; Yang, J. L., Influence of the number of layers on ultrathin $CsSnI_3$ perovskite: from electronic structure to carrier mobility. *Journal of Physics D-Applied Physics* **2018,** 51, 105101-105107.
49. Hao, F.; Stoumpos, C. C.; Guo, P.; Zhou, N.; Marks, T. J.; Chang, R. P.; Kanatzidis, M. G., Solvent-Mediated Crystallization of $CH_3NH_3SnI_3$ Films for Heterojunction Depleted Perovskite Solar Cells. *J Am Chem Soc* **2015,** 137, 11445-11452.
50. Noel, N. K.; Stranks, S. D.; Abate, A.; Wehrenfennig, C.; Guarnera, S.; Haghighirad, A.-A.; Sadhanala, A.; Eperon, G. E.; Pathak, S. K.; Johnston, M. B.; Petrozza, A.; Herz, L. M.; Snaith, H. J., Lead-free organic–inorganic tin halide perovskites for photovoltaic applications. *Energy Environ. Sci.* **2014,** 7, 3061-3068.
51. Eperon, G. E.; Leijtens, T.; Bush, K. A.; Prasanna, R.; Green, T.; Wang, J. T.; McMeekin, D. P.; Volonakis, G.; Milot, R. L.; May, R.; Palmstrom, A.; Slotcavage, D. J.; Belisle, R. A.; Patel, J. B.; Parrott, E. S.; Sutton, R. J.; Ma, W.; Moghadam, F.; Conings, B.; Babayigit, A.; Boyen, H. G.; Bent, S.; Giustino, F.; Herz, L. M.; Johnston, M. B.; McGehee, M. D.; Snaith, H. J., Perovskite-perovskite tandem photovoltaics with optimized band gaps. *Science* **2016,** 354, 861-865.
52. Hao, F.; Stoumpos, C. C.; Chang, R. P.; Kanatzidis, M. G., Anomalous band gap behavior in mixed Sn and Pb perovskites enables broadening of absorption spectrum in solar cells. *J Am Chem Soc* **2014,** 136, 8094-8099.
53. Li, L.; Zhang, F.; Hao, Y.; Sun, Q.; Li, Z.; Wang, H.; Cui, Y.; Zhu, F., High efficiency planar Sn–Pb binary perovskite solar cells: controlled growth of large grains via a one-step solution fabrication process. *Journal of Materials Chemistry C* **2017,** 5, 2360-2367.
54. Liao, W.; Zhao, D.; Yu, Y.; Shrestha, N.; Ghimire, K.; Grice, C. R.; Wang, C.; Xiao, Y.; Cimaroli, A. J.; Ellingson, R. J.; Podraza, N. J.; Zhu, K.; Xiong, R. G.; Yan, Y., Fabrication of Efficient Low-Bandgap Perovskite Solar Cells by Combining Formamidinium Tin Iodide with Methylammonium Lead Iodide. *J Am Chem Soc* **2016,** 138, 12360-12363.
55. Liu, C.; Fan, J.; Li, H.; Zhang, C.; Mai, Y., Highly Efficient Perovskite Solar Cells with Substantial Reduction of Lead Content. *Sci Rep* **2016,** 6, 35705-35712.
56. Yang, Z.; Rajagopal, A.; Chueh, C. C.; Jo, S. B.; Liu, B.; Zhao, T.; Jen, A. K., Stable Low-Bandgap Pb-Sn Binary Perovskites for Tandem Solar Cells. *Adv Mater* **2016,** 28, 8990-8997.
57. Zhao, D.; Yu, Y.; Wang, C.; Liao, W.; Shrestha, N.; Grice, C. R.; Cimaroli, A. J.; Guan, L.; Ellingson, R. J.; Zhu, K.; Zhao, X.; Xiong, R.-G.; Yan, Y., Low-bandgap mixed tin–lead iodide perovskite absorbers with long carrier lifetimes for all-perovskite tandem solar cells. *Nat Energy* **2017,** 2, 17018-17024.
58. Zuo, F.; Williams, S. T.; Liang, P. W.; Chueh, C. C.; Liao, C. Y.; Jen, A. K., Binary-metal perovskites toward high-performance planar-heterojunction hybrid solar cells. *Adv Mater* **2014,** 26, 6454-6460.
59. Rühle, S., Tabulated values of the Shockley–Queisser limit for single junction solar cells. *Solar Energy* **2016,** 130, 139-147.
60. Leijtens, T.; Prasanna, R.; Gold-Parker, A.; Toney, M. F.; McGehee, M. D., Mechanism of Tin Oxidation and Stabilization by Lead Substitution in Tin Halide Perovskites. *Acs Energy Letters* **2017,** 2, 2159-2165.
61. Wang, Y.-X.; Seng, K. H.; Chou, S.-L.; Wang, J.-Z.; Guo, Z.; Wexler, D.; Liu, H.-K.; Dou, S.-X., Reversible sodium storage via conversion reaction of a MoS2–C composite. *Chemical Communications* **2014,** 50, 10730-10733.
62. Marronnier, A.; Roma, G.; Boyer-Richard, S.; Pedesseau, L.; Jancu, J. M.; Bonnassieux, Y.; Katan, C.; Stoumpos, C. C.; Kanatzidis, M. G.; Even, J., Anharmonicity and Disorder in the Black Phases of Cesium Lead Iodide Used for Stable Inorganic Perovskite Solar Cells. *ACS Nano* **2018,** 12, 3477-3486.
63. Zhao, B.; Jin, S. F.; Huang, S.; Liu, N.; Ma, J. Y.; Xue, D. J.; Han, Q.; Ding, J.; Ge, Q. Q.; Feng, Y.; Hu, J. S., Thermodynamically Stable Orthorhombic gamma-$CsPbI_3$ Thin Films for High-Performance Photovoltaics. *J Am Chem Soc* **2018,** 140, 11716-11725.
64. Wang, Y.; Dar, M. I.; Ono, L. K.; Zhang, T.; Kan, M.; Li, Y.; Zhang, L.; Wang, X.; Yang, Y.; Gao, X.; Qi, Y.; Gratzel, M.; Zhao, Y., Thermodynamically stabilized beta-$CsPbI_3$-based perovskite solar cells with efficiencies >18. *Science* **2019,** 365, 591-595.
65. Sutton, R. J.; Filip, M. R.; Haghighirad, A. A.; Sakai, N.; Wenger, B.; Giustino, F.; Snaith, H. J., Cubic or Orthorhombic? Revealing the Crystal Structure of Metastable Black-Phase $CsPbI_3$ by Theory and Experiment. *ACS Energy Letters* **2018,** 3, 1787-1794.
66. Li, Z.; Yang, M.; Park, J.-S.; Wei, S.-H.; Berry, J. J.; Zhu, K., Stabilizing Perovskite Structures by Tuning Tolerance Factor: Formation of Formamidinium and Cesium Lead Iodide Solid-State Alloys. *Chemistry of Materials* **2016,** 28, 284-292.
67. Lu, M.; Zhang, X.; Bai, X.; Wu, H.; Shen, X.; Zhang, Y.; Zhang, W.; Zheng, W.; Song, H.; Yu, W. W.; Rogach, A. L., Spontaneous Silver Doping and Surface Passivation of $CsPbI_3$ Perovskite Active Layer Enable Light-Emitting Devices with an External Quantum Efficiency of 11.2%. *ACS Energy Letters* **2018,** 3, 1571-1577.
68. Shi, D.; Adinolfi, V.; Comin, R.; Yuan, M.; Alarousu, E.; Buin, A.; Chen, Y.; Hoogland, S.; Rothenberger, A.; Katsiev, K.; Losovyj, Y.; Zhang, X.; Dowben, P. A.; Mohammed, O. F.; Sargent, E. H.; Bakr, O. M., Solar cells. Low trap-state density and long carrier diffusion in organolead trihalide perovskite single crystals. *Science* **2015,** 347, 519-522.
69. Zheng, X.; Chen, B.; Dai, J.; Fang, Y.; Bai, Y.; Lin, Y.; Wei, H.; Zeng, Xiao C.; Huang, J., Defect passivation in hybrid perovskite solar cells using quaternary ammonium halide anions and cations. *Nat Energy* **2017,** 2, 17102-17110.
70. Chen, Q.; Zhou, H.; Song, T.-B.; Luo, S.; Hong, Z.; Duan, H.-S.; Dou, L.; Liu, Y.; Yang, Y., Controllable Self-Induced Passivation of Hybrid Lead Iodide Perovskites toward High Performance Solar Cells. *Nano Letters* **2014,** 14, 4158-4163.
71. Duong, T.; Wu, Y.; Shen, H.; Peng, J.; Fu, X.; Jacobs, D.; Wang, E.-C.; Kho, T. C.; Fong, K. C.; Stocks, M.; Franklin, E.; Blakers, A.; Zin, N.; McIntosh, K.; Li, W.; Cheng, Y.-B.; White, T. P.; Weber, K.; Catchpole, K., Rubidium Multication Perovskite with Optimized Bandgap for Perovskite-Silicon Tandem with over 26% Efficiency. *Adv Energy Mater* **2017,** 7, 1700228-1700238.
72. Shao, Y.; Fang, Y.; Li, T.; Wang, Q.; Dong, Q.; Deng, Y.; Yuan, Y.; Wei, H.; Wang, M.; Gruverman, A.; Shield, J.; Huang, J., Grain boundary dominated ion migration in polycrystalline organic–inorganic halide perovskite films. *Energy & Environmental Science* **2016,** 9, 1752-1759.

73. Snaith, H. J.; Abate, A.; Ball, J. M.; Eperon, G. E.; Leijtens, T.; Noel, N. K.; Stranks, S. D.; Wang, J. T.; Wojciechowski, K.; Zhang, W., Anomalous Hysteresis in Perovskite Solar Cells. *J Phys Chem Lett* **2014,** 5, 1511-1515.
74. Neophytou, M.; Griffiths, J.; Fraser, J.; Kirkus, M.; Chen, H.; Nielsen, C. B.; McCulloch, I., High mobility, hole transport materials for highly efficient PEDOT:PSS replacement in inverted perovskite solar cells. *Journal of Materials Chemistry C* **2017,** 5, 4940-4945.
75. Labban, A. E.; Chen, H.; Kirkus, M.; Barbe, J.; Del Gobbo, S.; Neophytou, M.; McCulloch, I.; Eid, J., Improved Efficiency in Inverted Perovskite Solar Cells Employing a Novel Diarylamino-Substituted Molecule as PEDOT:PSS Replacement. *Adv Energy Mater* **2016,** 6, 1502101-1502105.
76. Norrman, K.; Madsen, M. V.; Gevorgyan, S. A.; Krebs, F. C., Degradation patterns in water and oxygen of an inverted polymer solar cell. *J Am Chem Soc* **2010,** 132, 16883-16892.
77. Prasanna, R.; Leijtens, T.; Dunfield, S. P.; Raiford, J. A.; Wolf, E. J.; Swifter, S. A.; Werner, J.; Eperon, G. E.; de Paula, C.; Palmstrom, A. F.; Boyd, C. C.; van Hest, M. F. A. M.; Bent, S. F.; Teeter, G.; Berry, J. J.; McGehee, M. D., Design of low bandgap tin–lead halide perovskite solar cells to achieve thermal, atmospheric and operational stability. *Nat Energy* **2019,** 4, 939-947.
78. Zhou, W.; Zhao, Y.; Zhou, X.; Fu, R.; Li, Q.; Zhao, Y.; Liu, K.; Yu, D.; Zhao, Q., Light-Independent Ionic Transport in Inorganic Perovskite and Ultrastable Cs-Based Perovskite Solar Cells. *The Journal of Physical Chemistry Letters* **2017,** 8, 4122-4128.
79. Zhang, J.; Jin, Z.; Liang, L.; Wang, H.; Bai, D.; Bian, H.; Wang, K.; Wang, Q.; Yuan, N.; Ding, J., Iodine - Optimized Interface for Inorganic $CsPbI_2Br$ Perovskite Solar Cell to Attain High Stabilized Efficiency Exceeding 14%. *Advanced Science* **2018,** 5, 1801123-1801130.
80. Wang, Y.; Zhang, T.; Xu, F.; Li, Y.; Zhao, Y., A facile low temperature fabrication of high performance $CsPbI_2Br$ all - inorganic perovskite solar cells. *Solar RRL* **2018,** 2, 1700180-1700185.

For Table of Contents Only

A tin-lead alloyed low bandgap (~1.34 eV) inorganic perovskite has been reported to attain efficiencies up to 9.41% (stabilized-PCE 7.23%) and 7.60% (stabilized-PCE 7.31%) in full-structured and HTM-free perovskite solar cells, respectively, which are the highest efficiencies to date for all-inorganic perovskites with a bandgap below 1.40 eV.